International Journal of GEOMATE, Sept., 2021, Vol.21, Issue 85, pp.1-9
ISSN: 2186-2982 (P), 2186-2990 (O), Japan, DOI: https://doi.org/10.21660/2021.85.j2228
Geotechnique, Construction Materials and Environment

A PROCEDURE TO DETERMINE MATERIAL PARAMETERS BASED ON BOREHOLE DATA IN DYNAMIC ANALYSIS

*Tomohide Takeyama[1], Kazuya Honda[2], Shinya Tachibana[3] and Atsushi Iizuka[3]

[1]Department of Civil Engineering, Kobe University, Japan
[2]Tokyo Electric Power Services Co., Ltd., Japan
[3]Research Center for Urban Safety and Security, Kobe University, Japan

*Corresponding Author, Received: 07 June 2021, Revised: 25 June 2021, Accepted: 26 July 2021

ABSTRACT: Recently, the occurrence of large earthquakes has become a concern in Japan, prompting the need for a numerical method that can accurately predict real phenomena, such as the elastoplastic soil-water coupled finite element method. Because the elastoplastic constitutive model requires many material parameters, various soil tests and specialized knowledge are needed to determine these material parameters. In this study, a new method was proposed to determine the material parameters from the limited ground information obtained by borehole inspections and the method was validated by comparing the numerical results with monitored seismic behavior. One-dimensional seismic analyses were conducted using the material parameters estimated from borehole data near the target sites. It was confirmed that the amplitude and predominant period obtained by numerical simulation were consistent with the monitored data. As a result, it was found that the dynamic numerical result was more consistent with the monitored data when the compression index was set to be larger than that in the static analysis.

Keywords: Elastoplastic constitutive model, Soil-water coupled problem, Finite Element Method, Compression index

1. INTRODUCTION

In recent years, there have been concerns about the occurrence of large-scale earthquakes in Japan. Because earthquake disasters are difficult to predict, it is necessary to take sufficient preventive measures against them. However, the degree of damage caused by earthquakes depends largely on the scale of the earthquake, the region where the earthquake occurs, and the timing of the earthquake. Therefore, it is necessary to evaluate the risk of damage and take appropriate measures against possible earthquake disasters. Earthquakes cause various types of damage, such as building destruction, tsunamis, and landslides. In this study, a finite element method was used to simulate the liquefaction damage caused by an earthquake. Liquefaction damage rarely leads to direct human suffering. However, foundation ground deformation due to liquefaction can cause catastrophic damage to structures, which, in turn, can lead to prolonged recovery times. Therefore, liquefaction is a damage that causes significant economic losses.

Many local governments have prepared hazard maps for liquefaction risk. A simple assessment method for liquefaction risk based on FL (liquefaction resistance factor) and PL (liquefaction potential factor) [1] is often used to produce hazard maps. The FL and PL values are mainly evaluated by the N value, grain size, and surface seismic intensity of the target earthquake. In recent years, liquefaction damage has been observed in a wide range of areas after the 2011 off the Pacific Coast of Tohoku Earthquake. Ref.[2] compared the liquefaction risk based on the FL and PL values with the actual liquefaction damage in the 2011 off the Pacific Coast of Tohoku Earthquake. They found that liquefaction damage was not observed in areas where liquefaction risk was considered to be low by the FL and PL values. However, there were many sites where no liquefaction was found, even though the sites were considered to be at high risk of liquefaction. An overestimation of liquefaction risk may increase the cost of the preventive measures, reduce the reliability of estimates, and weaken the sense of crisis.

One of the detailed liquefaction analysis methods is effective stress analysis, which employs the elastoplastic constitutive model. Effective stress analysis is a method that considers the interaction between soil particles and pore water, and it simulates liquefaction by directly expressing the decrease in effective stress. Therefore, this method can evaluate liquefaction risk more accurately than conventional methods. However, elastoplastic analysis requires many material parameters, and various soil tests and expertise are necessary to determine the parameters. This makes it difficult to set appropriate material parameters, which is one of the reasons why simple liquefaction assessment methods are widely used. To assess the liquefaction risk in a wide area, such as a hazard map, it is very costly to determine the material parameters for each location by conducting the necessary soil tests. Therefore, in this study, we used a method to mechanically determine the material parameters from limited ground information. Iizuka and Ohta [3] and Miyata [4] developed a method to determine the material parameters that are necessary for elastoplastic constitutive models based on limited ground information. Ref. [3] proposed a method for determining the parameters from the plasticity index for clayey soils. Ref. [4] proposed a method to determine the material parameters from the N values for sandy soils. A large amount of borehole data has accumulated over the years in Japan. Local governments and the Ministry of Land, Infrastructure, Transport and Tourism (MLIT) have made accumulated borehole data available to the public. The borehole data contained mainly N values and soil classifications for each depth. The borehole data are formatted in the extended markup language (XML) format, which makes it relatively easy to handle even if the amount of data is large. Therefore, borehole data are considered as a suitable source for determining the material parameters needed for the elastoplastic analysis of the soil. In this study, the material parameters were determined based on borehole data, and elastoplastic dynamic analyses were performed. Furthermore, the applicability of the parameter determination method to the actual field was validated by comparing the observed waveforms with the analytical results.

Figs. 1 and 2 illustrate the parameter determination flow [2, 3], and consist of theoretical equations and empirical equations obtained from experiments. In general, the loading speed in soil tests differs greatly from the loading speed that the ground is subjected to in actual earthquakes. Because the strength of geomaterials increases as the loading speed increases, using the parameters determined from these empirical equations will underestimate the strength. Several experiments have been conducted using triaxial compression tests to determine the relationship between strength and loading speed. Casagrande and Shannon [5] conducted triaxial compression tests on dry sand at several loading rates and found that the shear strength tended to increase with increasing loading rate. Seed and Lundgren [6] conducted triaxial compression tests on saturated sand at several loading rates under drained and undrained conditions, and showed a trend of increased shear strength at higher loading rates. Lee et al. [7] conducted triaxial compression tests on dry sand under different confining pressures at several loading rates and found that the trend of increase in shear strength at higher loading rates was different depending on the confining pressure.

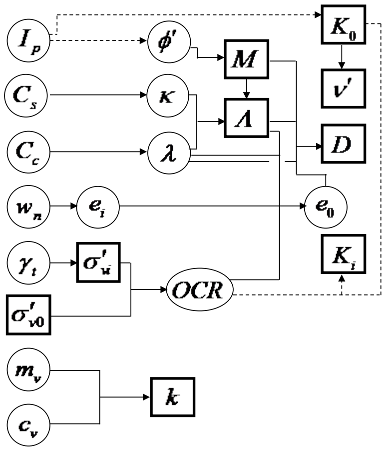

$$(1)\quad \sin\phi' = 0.81 - 0.233\log I_p$$

$$(2)\quad M = 6\sin\phi' / (3 - \sin\phi')$$

$$\Lambda = \mathrm{M}/1.75$$

$$(4)\quad K_0 = 0.44 + 0.0042 I_p$$

$$(5)\quad \nu' = K_0/(1 + K_0)$$

$$(6)\quad \kappa = 0.434 C_s$$

$$(7)\quad \lambda = 0.434 C_c$$

$$(8)\quad \Lambda = 1 - \kappa/\lambda$$

$$(9)\quad e_i = G_s w_n$$

$$(10)\quad OCR = \sigma'_{v0}/\sigma'_{vi}$$

$$(11)\quad e_0 = e_i - \lambda(1 - \Lambda)\ln(\overline{OCR})$$

$$(12)\quad D = \lambda\Lambda / M(1 + e_0)$$

$$(13)\quad K_i = K_0(OCR)^{0.54\exp(-I_p/122)}$$

$$(14)\quad k = m_v c_v \gamma_w$$

Fig.1 Material parameter determination flow from plasticity index

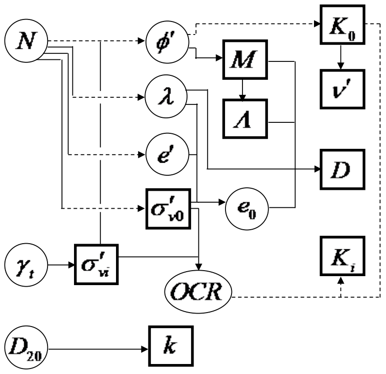

$$(1)\quad \phi' = 1.85\left(\frac{N}{(\sigma'_{vi}/98) + 0.7}\right)^{0.6} + 26$$

$$(2)\quad \lambda = -0.016\ln N + 0.08$$

$$(3)\quad e' = -0.15\ln N + 1.0$$

$$(4)\quad \sigma'_{v0} = 40N$$

$$(5)\quad M = 6\sin\phi' / (3 - \sin\phi')$$

$$(6)\quad \Lambda = M/1.75$$

$$(7)\quad K_0 = 1 - \sin\phi'$$

$$(8)\quad \nu' = K_0/(1 + K_0)$$

$$(9)\quad OCR = \sigma'_{v0}/\sigma'_{vi}$$

$$(10)\quad e_0 = e' - \lambda\ln(\sigma'_{v0}/98)$$

$$(11)\quad D = \lambda\Lambda / M(1 + e_0)$$

$$(12)\quad K_i = K_0(OCR)^{\sin\phi'}$$

$$(13)\quad k = 0.0034 D_{20}^{2.2954}$$

Fig.2 Material parameter determination flow from N-value

Watanabe [8] conducted triaxial compression tests under saturated drainage conditions at various loading rates and showed that the stiffness tends to increase at higher loading rates because the behavior is closer to that under undrained conditions. In the parameter determination flow [3,4], the relationship based on the consolidation test is adopted as the empirical equation for estimating the compression index. Because the consolidation test is conducted at a very slow loading rate, it may underestimate the stiffness of the soil during an earthquake. In this study, we proposed a method to estimate the compression index, λ, based on the relationship between Young's modulus E and N value, which is defined in various design guidelines. Then, a parameter determination method applicable to dynamic analysis was developed by combining it with existing parameter determination methods.

2. NUMERICAL MODEL

In this study, an elastoplastic dynamic analysis was performed considering the interaction between soil particles and pore water. The soil-water coupled elastoplastic finite element program DACSAR-I developed [9] was used. In this section, the governing equations and the constitutive model used in the program are described.

2.1 Governing Equations

The governing equations are as follows:

$$\rho\ddot{\boldsymbol{u}} + \nabla\cdot\boldsymbol{\sigma} - \rho\boldsymbol{b} = 0\,, \tag{1}$$

$$\dot{\varepsilon}_v - \nabla\cdot\boldsymbol{w} - \frac{n}{K_w}\dot{p}_w = 0\,, \tag{2}$$

$$\boldsymbol{\sigma} = \boldsymbol{\sigma}' + p_w\boldsymbol{1}\,, \tag{3}$$

$$\dot{\boldsymbol{\sigma}}' = \boldsymbol{C} : \dot{\boldsymbol{\varepsilon}}\,, \tag{4}$$

$$\boldsymbol{\varepsilon} = -(\nabla\otimes\boldsymbol{u} + \boldsymbol{u}\otimes\nabla)/2\,, \tag{5}$$

$$\boldsymbol{w} = -\boldsymbol{k}\cdot\nabla h\,. \tag{6}$$

Eqs. (1) and (2) represent the conservation of momentum and the conservation of mass, respectively. Eqs. (4) - (7) are the principal of effective stress, the constitutive equation, the strain-displacement relation and the Darcy's law. ρ is the density of soil, $\boldsymbol{u}$ the displacement vector, $\boldsymbol{\sigma}$ the stress tensor, $\boldsymbol{b}$ the body force vector, ε_v the volumetric strain, $\boldsymbol{w}$ the Darcy's velocity, n the porosity, K_w the bulk modulus of pore water, p_w the pore water pressure, $\boldsymbol{\sigma}'$ the effective stress tensor, $\boldsymbol{1}$ the second order identity tensor, $\boldsymbol{C}$ the constitutive tensor, $\boldsymbol{\varepsilon}$ the strain tensor, $\boldsymbol{k}$ the hydraulic conductivity tensor, h the total water head. Note that the compression is defined as positive. By solving the governing equations, for given boundary and initial conditions, displacement $\boldsymbol{u}$ and pore water pressure p_w can be obtained.

2.2 Constitutive Model

The constitutive model employed in the analysis was based on the EC model [10]. The yield function of the EC model is expressed as follows:

$$f = \mathrm{M}D\ln\frac{p'}{p'_0} + \frac{\mathrm{M}D}{n_E}\left(\frac{\eta^*}{\mathrm{M}}\right)^{n_E} - \varepsilon_v^p = 0 \tag{7}$$

where M is the critical state parameter, D is the coefficient of dilatancy [11], p' is the effective mean stress, p'_0 is the effective mean stress in the pre-consolidated state, ε_v^p is the plastic volumetric strain, n_E is the parameter used to fit the contractancy response of the EC model to the experimental results, and η^* is the generalized stress ratio.

The EC model was combined with the extended subloading surface model, rotationally hardening model, and shear hardening/softening model [12, 13] to describe the cyclic behavior of the soil due to earthquakes. The extended subloading surface with aforementioned hardening rules is given as

$$\bar{f} = \mathrm{M}D\ln\frac{\overline{p}'}{p'_0} + \frac{\mathrm{M}D}{n_E}\left(\frac{\overline{\eta}^*}{\mathrm{M}}\right)^{n_E} - MD\ln R - H = 0 \tag{8}$$

where $\overline{\boldsymbol{\sigma}}' = \boldsymbol{\sigma}' - (1-R)\boldsymbol{\alpha}$ is the modified effective stress with $\boldsymbol{\alpha}$ the similarity center of the subloading surface, R is the similarity ratio of subloading surface with respect to the normal yield surface, H is the hardening parameter for representing the shear induced hardening/softening. $\overline{p}'$ and $\overline{\eta}^*$ are the effective mean stress and the generalized stress ratio in terms of the modified effective stress. The generalized stress ratio is expressed as

$$\overline{\eta}^* = \sqrt{\frac{3}{2}}\left\|\overline{\boldsymbol{\eta}} - \boldsymbol{\eta}_e\right\| \tag{9}$$

where $\overline{\boldsymbol{\eta}} = \overline{\boldsymbol{s}}/\overline{p}'$ the stress ratio tensor, and $\boldsymbol{\eta}_e$ is the stress ration tensor represents stress anisotropy. The developing laws for R, $\boldsymbol{\alpha}$, $\boldsymbol{\eta}_e$ and H are as follows:

$$\dot{R} = -\frac{m}{D}\ln R\left\|\dot{\boldsymbol{\varepsilon}}^p\right\|\,, \tag{10}$$

$$\dot{\boldsymbol{\alpha}} = c\left\|\dot{\boldsymbol{\varepsilon}}^p\right\|(\boldsymbol{\sigma}' - \boldsymbol{\alpha}) + \frac{1}{p'_c}\left\{\dot{p}'_c - \dot{\boldsymbol{\eta}}_e\frac{\partial f_\alpha}{\partial\boldsymbol{\eta}_e}\right\}\boldsymbol{\alpha}\,, \tag{11}$$

$$\dot{\boldsymbol{\eta}}_e = \frac{b_r}{D}\left\{M_r(\boldsymbol{\eta} - \boldsymbol{\eta}_e) - \left\|\boldsymbol{\eta} - \boldsymbol{\eta}_e\right\|\boldsymbol{\eta}_e\right\}\left\|\dot{\boldsymbol{\varepsilon}}_d^p\right\|\,, \tag{12}$$

$$\dot{H} = \dot{\varepsilon}_v^p + \sqrt{2/3}\,\mu\left\|\dot{\boldsymbol{\varepsilon}}_d^p\right\|(\eta - M_d)\,, \tag{13}$$

in which m is the parameter which controls the speed of the subloding surface to approach the normal yield surface, c the parameter which controls the speed of the similarity center. b_r is the parameter which controls the rotational speed of yield surface. M_r is the parameter which defined the rotational limit of the yield surface. μ is the parameter controls the contribution of the shear and M_d defines the boundary of the hardening and softening.

Numerical methods have been used to analyze seismic response. Ref. [14] does not take the interaction between soil and water into account. Ref. [15] used a simple model instead of an elastoplastic model. Refs. [16, 17] use the similar numerical model to this study. The main difference is the constitutive model.

3. EQUATION TO ESTIMATE COMPRESSION INDEX

The normal consolidation line is expressed as

$$de = -\lambda \frac{dp'}{p'} \tag{14}$$

from the linearity in e-logp' relationship, where e is void ratio, λ is compression index, and p' is effective mean stress. From the definition of bulk modulus: $K=dp'/d\varepsilon_v$ and the relationship between volumetric strain ε_v and void ratio: $d\varepsilon_v = -de/(1+e_0)$, the following equation was derived.

$$K = \frac{1+e_0}{\lambda} p' \tag{15}$$

where e_0 is the void ratio in the pre-consolidated state. The shear modulus G was expressed as follows:

$$G = \mu K\ ,\ \ \mu = \frac{3(1-2\nu')}{2(1+\nu')} \tag{16}$$

for the linear elastic model, where ν' is Poisson's ratio in terms of the effective stress. By substituting Eq. (16) into Eq. (15) and noting the relationship between shear modulus G and shear wave velocity V_s: $G=\rho V_s{}^2$, the compression index λ is expressed as

$$\lambda = \frac{\mu(1+e_0)}{\rho V_s^2} p' \tag{17}$$

where ρ is the density of soil. The effective mean stress p' can be obtained from the overburden pressure and the coefficient of earth pressure. The Poisson's ratio ν' and the void ratio e_0 can be estimated according to Figs. 1 and 2. In the specifications for highway bridges [18], the shear wave velocity is estimated from the N value using the following equation:

$$V_s = 100N^{1/3} \quad (1 \le N \le 25) \quad \text{for clay} \tag{18}$$

$$V_s = 80N^{1/3} \quad (1 \le N \le 50) \quad \text{for sand} \tag{19}$$

In this research, the shear wave velocity is estimated by Eqs. (18) and (19), and it is assumed that the estimated shear wave velocity is in the pre-consolidated state.

4. OVERVIEW OF ANALYSIS

In this study, the seismic waveforms from vertical array observations in Tokyo was focused on. The method for determining the material parameters was based on the parameter determination flow [3]. A one-dimensional elastoplastic dynamic analysis of the observed waveforms at each location was performed to confirm whether the propagation of the waves could be represented on the actual ground. The information on the three observation points and earthquakes used in the numerical simulation are summarized in Table 1 and Table 2, respectively.

Table 1 Information on points where the strong-motion was observed

Point	Site	Latitude Longitude	Depth
1	Shinkiba	35.636°N 139.837°E	65 m
2	Wakasu	35.629°N 139.836°E	60 m
3	Yashio	35.605°N 139.761°E	51 m

Table 2 Information on input earthquakes

Event	Epicenter	Date and time
1	Off the Fukusima	Aug. 4, 2019 19:23
2	Off the Chiba	Oct. 12, 2019 18:21
3	Northwest of Chiba	Oct. 31, 2019 11:06

The input accelerations of Events 1–3 are shown in Figs 3-5. The observation records used in this study are available on the website of the "Strong-Motion Earthquake Records in Japanese Ports" operated by the Ports and Harbors Bureau, Ministry of Land, Infrastructure, and Transport. The ground information for the sites is based on the N values

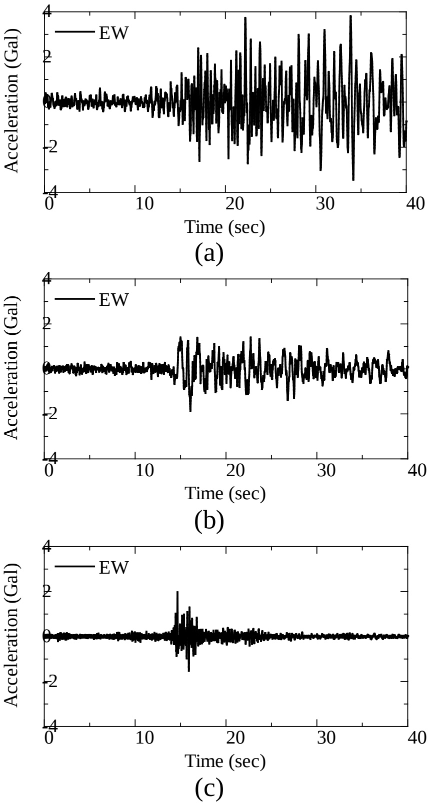

(a)

(b)

(c)

Fig.3 Input acceleration waveform of (a) Event 1, (b) Event 2, (c) Event 3 at Point 1

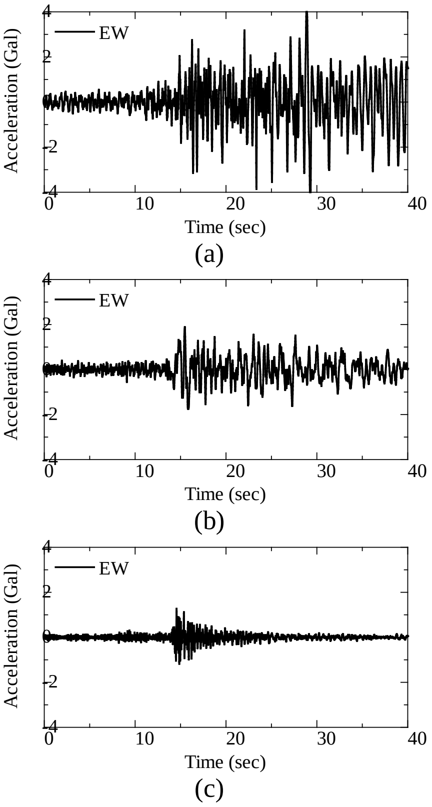

(a)

(b)

(c)

Fig.4 Input acceleration waveform of (a) Event 1, (b) Event 2, (c) Event 3 at Point 2

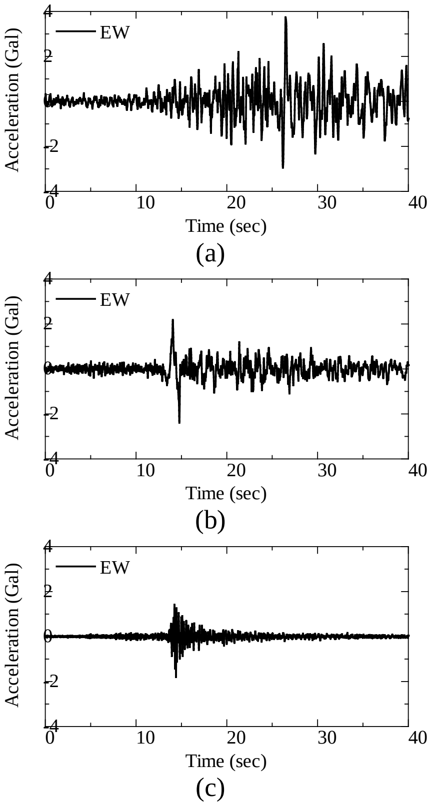

(a)

(b)

(c)

Fig.5 Input acceleration waveform of (a) Event 1, (b) Event 2, (c) Event 3 at Point 3

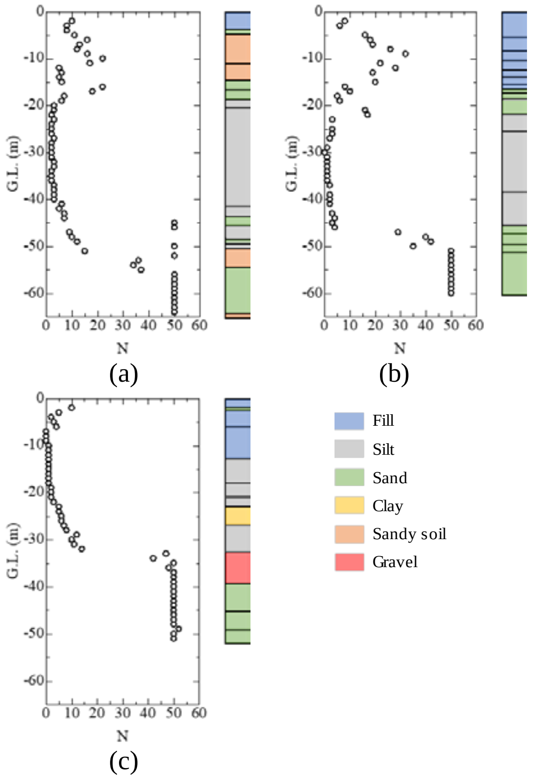

(a)

(b)

(c)

Fig.6 Borehole data, distribution of N value and soil classification in depth (a) Point 1, (b) Point 2, (c) Point 3 and soil classifications of the observation points listed on the same website. Fig. 6 shows the distribution of N values and soil classifications at points 1–3. In addition to the N value, the unit weight of the soil, plasticity index, and hydraulic conductivity must be specified. In this study, the results of soil tests in the liquefaction prediction report published by the Tokyo Metropolitan Government (2013) were used as a reference for each soil category, as shown in Tables 3 and 4. Hydraulic conductivity was specified as a general value for each soil category with reference to the Japanese Geotechnical Society Standards [19]. Here, the waves observed at the ground surface consist of real waves propagating inside the ground and surface waves propagating at the ground surface. In the numerical simulations, only real waves propagating from the ground were calculated, so it was not possible to simply compare the calculated and measured values. Surface waves are typically observed in real waves. Therefore, the observed waveforms up to the first 40 s were considered in the simulations because the influence of surface waves was small for the first 40 s.

Table 3 Applied parameters for clayey soil

Classification of soil	γ_t (kN/m^3)	I_p	k (m/s)
Clay, Mud	15.7	31	1.0×10^{-8}
Silt	17.5	15	1.0×10^{-6}
Organic soil, Peat	12.9	90	1.0×10^{-6}
Volcanic soil, Loam	13.6	54	1.0×10^{-4}

Note: γ_t is unit weight of soil, I_p is Plasticity index, and k is coefficient of permeability

Table 4 Applied parameters for sandy soil

Classification of soil	γ_t (kN/m^3)	I_p	k (m/s)
Sand	19.0	-	1.0×10^{-4}
Gravel	20.1	-	1.0×10^{-2}
Backfill, Embankment, Waste	17.8	-	1.0×10^{-6}

Note: γ_t is unit weight of soil, I_p is Plastic index, and k is coefficient of permeability

5. CONDITIONS OF THE ANALYSIS

The parameters specific to each plastic hardening model were empirically set, as shown in Table 5.

Table 5 Parameters for the plastic hardening models

Classification of soil	n_E	m	c	μ	M_d	b_r	M_r
Clayey soil	1.5	0.1	10	-	-	1.0	0.5
Sandy soil	1.2	0.1	30	2.0	0.8	1.0	0.5

The finite element mesh is a one-dimensional vertical column with 1.0 m spacing in the depth direction. To represent semi-infinite horizontal stratified ground, both sides of a vertical column were considered periodic boundary conditions. The behavior during an earthquake was assumed to occur in a very short period of time during which there was no water movement, while both sides and the bottom of the vertical column were assumed to be undrained. For the top surface, drainage conditions were assumed to be the ground surface. The observed waveforms at each point were given as the boundary conditions at the bottom, and represent the behavior below the input depth. The simulated acceleration was compared with the observed acceleration at each location. The viscous boundary conditions were also set to suppress the reflection of seismic waves at the bottom. In this analysis method, the Rayleigh damping was introduced to increase the stability of the calculation.

6. RESULTS OF THE ANALYSIS

As a result of the analysis, the observed waveforms at the ground surface were compared with the acceleration waveforms at the ground surface obtained from the analysis. Fig. 7 illustrates the acceleration waveforms of the case of Event 1 at Point 1, and Figs. 8–10 illustrate the Fourier spectra of each case. The spectra were smoothed with a Parzen window with a bandwidth of 0.1 Hz.

From Fig. 7, comparing the acceleration waveforms of Event 1 at Point 1, the actual phases of the EW directions can be roughly represented, and the trend of seismic wave propagation in the ground can be expressed. A comparison of the Fourier spectra in Figs. 8–10 shows that, in many cases, the actual predominant period can be approximately represented. In Event 3 (the earthquake in the northwestern part of Chiba prefecture), a component with a small period of less than 0.5 s is dominant at all points, and the analysis estimated a larger predominant period than the actual measurement. For earthquakes with very small predominant periods, the predominant period cannot be accurately estimated.

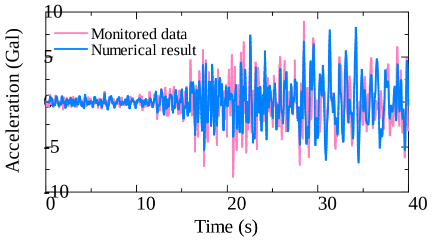

Fig.7 Time history of acceleration at ground surface of Event 1 at Point 1

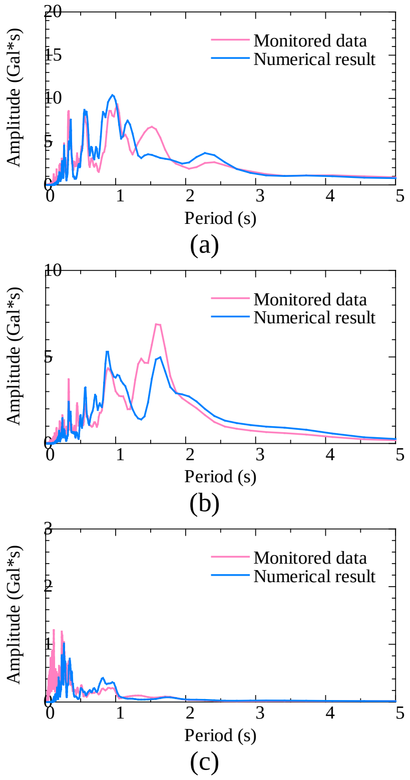

(a)

(b)

(c)

Fig.8 Fourier spectra of acceleration at ground surface of (a) Event 1, (b) Event 2, (c) Event 3 at Point 1

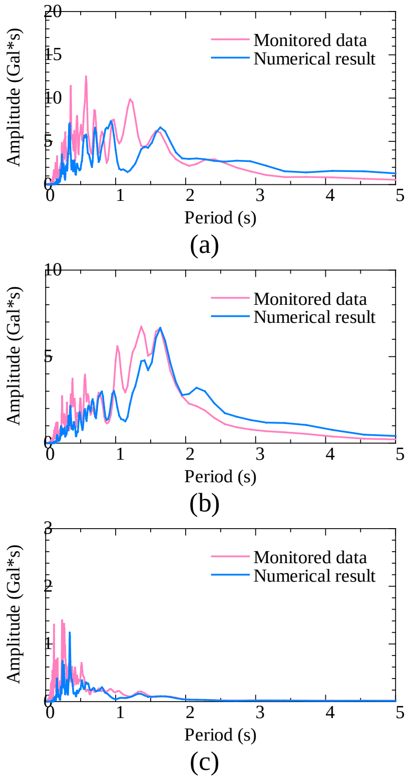

(a)

(b)

(c)

Fig.9 Fourier spectra of acceleration at ground surface of (a) Event 1, (b) Event 2, (c) Event 3 at Point 2

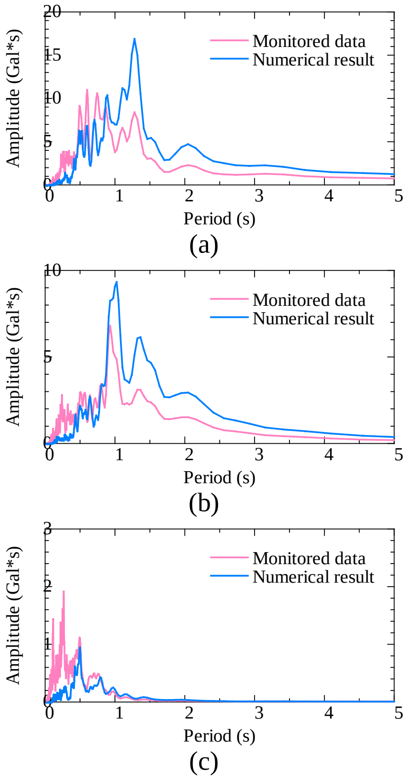

(a)

(b)

(c)

Fig.10 Fourier spectra of acceleration at ground surface of (a) Event 1, (b) Event 2, (c) Event 3 at Point 3

The spatial and temporal resolution may have an effect.

Next, it was compared that the difference in the results of the analysis between the case where the compression index, λ, is estimated based on the existing parameter determination flow (called the previous method) and the case where the compression index, λ, is estimated using the method introduced in this study (called the proposed method). Fig. 11 compares the Fourier spectra obtained from the previous method and the proposed method with the Fourier spectra of the observed waveform. Comparing the results in the EW direction, the proposed method is able to represent the spectra closer to the observed values than the previous method for all period components.

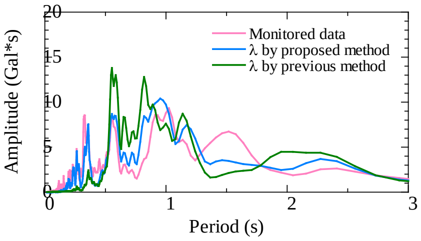

Fig.11 Fourier spectra of acceleration at ground surface of Event 1 at Point 1

In particular, the proposed method is able to express small-period components, which are almost impossible to express using the previous method. The amplitudes obtained from the proposed method were closer to the observed values than those obtained from the previous method. The same trend was obtained for other events and points.

7. CONCLUTION

In this study, a new formula to estimate the compression index was introduced into the existing parameter determination method. The method used in this study estimates the compression index based on the relationship between the N value and the elastic wave velocity described in the design standard, which is higher than the conventional empirical formula. Thus, the compression index is higher than that estimated from the conventional empirical equation, and this makes it suitable for expressing the compression index when the loading speed is high, such as in earthquakes. Using the parameters estimated by this method, the short-period component of the actual earthquake waveform can be represented more accurately. In addition, the phase of the acceleration waveforms is close to that of the actual acceleration waveforms on the ground surface, which means that the propagation of seismic waves can be calculated more accurately. However, waveforms with a period of less than 0.5 s could not accurately represent the actual behavior.

While the soil-water coupled finite element method and the constitutive model used in this study can represent the liquefaction process of the ground under cyclic shear (because the input seismic motions were small earthquakes with a maximum acceleration of less than 10 Gal), the excess pore water pressure did not increase enough to cause liquefaction. To assess the risk caused by liquefaction, it is necessary to verify whether the occurrence of liquefaction and the displacement caused by liquefaction can be accurately calculated by inputting earthquakes with higher acceleration. It should be noted that the influence of surface waves propagating on the ground surface increases when a large-scale earthquake is input.

8. ACKNOWLEDGMENTS

This work was supported by KAKENHI Grant-in-Aid for Scientific Research (C) #20K04682.

9. REFERENCES

[1] Iwasaki, T., Tatsuoka, F., Tokita, K., and Yasuda, S., Estimation of Degree of Soil Liquefaction during Earthquakes, The Japanese Society of Soil Mechanics and Foundation Engineering, Vol. 28, No. 4, 1980, pp.23-29 (in Japanese) .

[2] Sasaki, T., Ishihara, M., Tanimoto, S., and Masuyama, H., Study on Liquefaction Determining Method based on Liquefaction occurred by the 2011 off the Pacific Coast of Tohoku Earthquake, Technical Note of PWRI 4280, 2014.

[3] Iizuka, A., and Ohta, H., A Determination Procedure of Input Parameter in Elasto-Viscoplastic Finite Element Analysis, Soils and Foundations, Vol. 27, No. 3, 1987, pp.71-87.

[4] Miyata, T., Deformation and Stability of Sandy Soil during Excavation Work, Master’s thesis of Tokyo Institute of Technology, 2001.

[5] Casagrande, A., and Shannon, W. L., Stress-Deformation and Strength Characteristics of Soils under Dynamic Loads, Proceedings of the 2nd International Conference on Soil Mechanics and Foundation Engineering, 1948, pp.29-34.

[6] Seed, H. B. and Lundgren, R., Investigation of the Effect of Transient Loading on the Strength and Deformation Characteristics of Saturated Sands, Proceedings of the American Society for Testing and Materials, Vol. 54, 1954, pp.1288-1306.

[7] Lee, K. L, Seed, H. B., and Dunlop, P., Effect of Transient Loading on the Strength of Sand, Proceedings of the 7th International Conference on Soil Mechanics and Foundation Engineering, 1969, pp.239-247.

[8] Watanabe, K., The Effects of Loading Rate on Soil Behavior and Bearing Capacity in view of Seismic Design for Pile Foundation, Doctoral thesis of Tokyo Institute of Technology, 2015.

[9] Takeyama, T., Tachibana, S., and Furukawa, A., A Finite Element Method to describe the Cyclic Behavior of Saturated Soil, International Journal of Material Science and Engineering, Vol. 2, Issue 1, 2015, pp.20-25.

[10] Ohno, S., Iizuka, A., and Ohta, H., Two Categories of New Constitutive Model derived from Non-Linear Description of Soil Contractancy, Journal of Applied Mechanics, Vol. 9, 2006, pp.407-414.

[11] Shibata, T., On the Volume Changes of Normally Consolidated Clays, Annuals of Disaster Prevention Research Institute, Kyoto University, Vol. 6, 1963, pp.128-134.

[12] Hashiguchi, K., Subloading Surface Model in Unconventional Plasticity, International Journal of Soils and Structures, Vol.25, No. 8, 1989, pp.917-945.

[13] Hashiguchi, K., and Chen, Z. P., Elastoplastic Constitutive Equation of Soils with the Subloading Surface and the Rotational Hardening, International Journal for Numerical and Analytical Methods in Geomechanics, Vol.

22, No. 3, 1998, pp.197-227.

[14] Liang, F., Chen, H., and Huang, M., Accuracy of three-dimensional seismic ground response analysis in time domain using nonlinear numerical simulations, Earthquake Engineering and Engineering Vibration, Vol. 16, 2017, pp.487-498.

[15] Esmaeili, M., and Tavokoli, B., Finite element method simulation of explosive compaction in saturated loose sandy soils, Soil Dynamics and Earthquake Engineering, Vol. 116, 2019, pp.446-459.

[16] Tang, X., Zhang, X., and Uzuoka, R., Novel adaptive time stepping method and its application to soil seismic liquefaction analysis, Soil Dynamics and Earthquake Engineering, Vol. 71, 2015, pp.100-113.

[17] Bao, X., Xia, Z., Ye, G., Fu, Y., and Su, D., Numerical analysis on the seismic behavior of large metro subway tunnel in liquefiable ground, Tunneling and Under Ground Space Technology, Vol. 66, 2017, pp.91-106.

[18] Japan Road Association, Specification for Highway Bridge Part V Seismic Design, 1969.

[19] Japanese Geotechnical Society, Japanese Geotechnical Society Standards Laboratory Testing Standards of Geomaterials, 2000.